Photonic quantum metrology with variational quantum optical nonlinearities

A. Muñoz de las Heras,* C. Tabares, J. T. Schneider, L. Tagliacozzo, D. Porras, and A. González-Tudela
Institute of Fundamental Physics IFF-CSIC, Calle Serrano 113b, 28006 Madrid, Spain

(Received 26 September 2023; revised 1 December 2023; accepted 8 February 2024; published 19 March 2024)

Photonic quantum metrology harnesses quantum states of light, such as NOON or twin-Fock states, to measure unknown parameters beyond classical precision limits. Current protocols suffer from two severe limitations that preclude their scalability: the exponential decrease in fidelities (or probabilities) when generating states with large photon numbers due to gate errors and the increased sensitivity of such states to noise. Here, we develop a deterministic protocol combining quantum optical nonlinearities and variational quantum algorithms that provides a substantial improvement on both fronts. First, we show how the variational protocol can generate metrologically relevant states with a small number of operations which do not significantly depend on photon number, resulting in exponential improvements in fidelities when gate errors are considered. Second, we show that such states offer a better robustness to noise compared to other states in the literature. Since our protocol harnesses interactions already appearing in state-of-the-art setups, such as cavity QED, we expect that it will lead to more scalable photonic quantum metrology in the near future.

DOI: 10.1103/PhysRevResearch.6.013299

I. INTRODUCTION

Quantum metrology capitalizes on quantum resources to improve measurement precision beyond classical limits [1–7]. Classically, the estimation error of an unknown parameter φ using N probes is bound by the standard quantum limit (SQL) $\Delta\varphi \geqslant 1/\sqrt{N}$. However, entangled probes can offer a quadratic improvement over the SQL, reaching the so-called Heisenberg limit (HL) $\Delta\varphi = 1/N$. In the photonic scenario of phase estimation [8–11], quantum states of light such as NOON [12] or twin-Fock states (TFS), i.e., the same Fock state at each arm of a Mach-Zehnder interferometer (MZI) [13], overcome the SQL (even reaching the HL in the case of NOON states). Proof-of-principle experiments have already shown the potential of this approach, but so far restricted to up to five photons [14–16]. The underlying reason behind such low numbers is that photonic quantum metrology suffers from two limitations. (i) State-of-the-art methods to generate metrologically relevant states involve a number of operations [17–19] or interaction time [20,21] increasing with the number of photons. This ultimately yields an exponential fidelity decrease with photon number when gate errors are considered. A way of improving fidelities consists in using postselection [14,15,22–29], but at the price of vanishingly small probabilities with a growing photon number. (ii) The resource entangled states, such as NOON ones, suffer from an increased sensitivity to noise, e.g., decoherence and photon loss in the channel, spoiling their quantum advantage even if generated accurately. Thus innovative ideas are required to scale photonic quantum metrology protocols beyond proof-of-principle realizations.

Recently, variational quantum algorithms (VQAs) [30,31] have emerged as a tool to make the best out of current quantum hardware, which is noisy and thus can perform a limited number of coherent operations. The key idea of these hybrid algorithms is to use a classical optimizer to find the set of parameters of a parametrized quantum circuit (PQC) implemented on the hardware such that it minimizes a given cost function. Recent works on spin systems have shown how these VQAs can also be useful in the context of quantum metrology [32–40], e.g., by using the quantum Fisher information (QFI) [37–39] as cost function. However, in the photonic context this potential of variational approaches for quantum metrology has been scarcely explored and limited to either linear systems [41,42] or PQCs with fixed nonlinearities [43].

In this work, we combine VQAs with state-of-the-art quantum optical nonlinearities to design an algorithm that overcomes the limitations of current protocols. In particular, we consider two types of PQCs (the *Ansätze*) each formed by two coupled cavity systems but featuring different types of nonlinearities: the coupling to a two-level system that appears in cavity QED and a Kerr-type one. Our method employs the QFI as cost function to find the optimal parameters that transform unentangled coherent states into states that approximately saturate the HL. Importantly, we find that the number of operations required is independent of the photon number with both types of nonlinearities, which guarantees that the fidelity of the generated states will not decrease with the photon number, unlike in existing protocols. For the two *Ansätze*, we consider the impact of noise and show that the generated states feature a larger robustness than NOON and TFS. In a second step of the VQA, we consider photon number measurements

*alberto.munoz@iff.csic.es

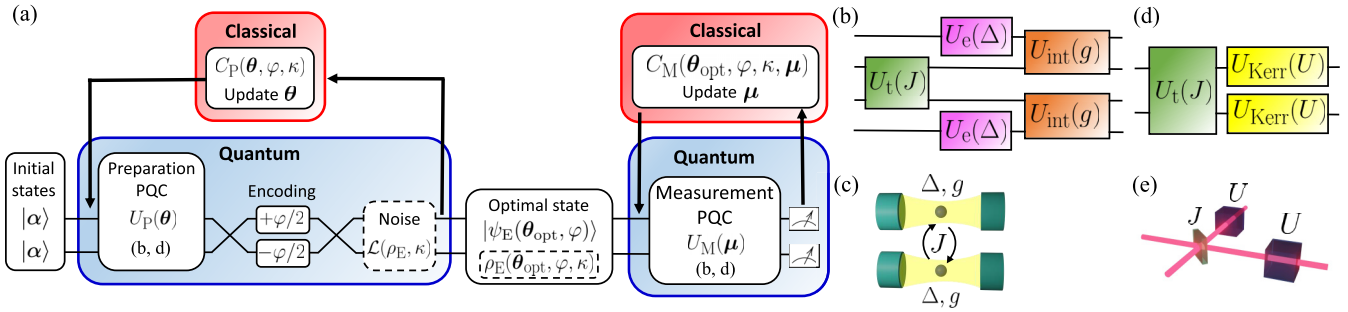

FIG. 1. (a) Overview of the variational optimization protocol. Two identical coherent states $|\alpha\rangle$ are the input of a variational quantum algorithm (VQA) aimed at finding the optimal state for the estimation of a phase φ. This consists of a quantum part including a parametrized quantum circuit (PQC) described by a unitary U_P, a Mach-Zehnder interferometer (MZI) encoding the phase difference between its two arms, and (optionally) a nonunitary evolution accounting for noise with decay rate κ described by a Lindbladian $\mathcal{L}$ acting on the density matrix of the system ρ_E. The classical part of the VQA is an optimizer that changes the parameters $\boldsymbol{\theta}$ of the PQC in search of the minimum of the cost function C_P. The resulting optimal state $|\psi_E\rangle$ (ρ_E in the noisy case) evaluated at the optimal parameters $\boldsymbol{\theta}_{opt}$ is the input of the second part of the VQA, which employs the PQC to prepare optimal measurements as well as a classical optimizer that aims at minimizing the cost function C_M by varying the parameters $\boldsymbol{\mu}$ of the second PQC. (b) A single layer of the emitters *Ansatz*, consisting of a tunneling unitary U_t depending on the tunneling amplitude J, a detuning unitary U_e for each mode depending on the cavity-emitters detuning Δ, and an interaction unitary U_{int} for each mode depending on the light-matter coupling strength g. The upper and lower modes of the scheme correspond to the emitters, while the two central ones are the photonic modes. (c) A possible implementation of the emitters *Ansatz* in a cavity-QED setup. (d) A single layer of the Kerr *Ansatz*, consisting of a tunneling unitary U_t depending on the tunneling amplitude J and a Kerr unitary U_{Kerr} for each mode depending on the nonlinearity strength U. (e) A possible implementation of the Kerr *Ansatz* in a photonic setup.

and maximize the classical Fisher information (CFI) to find the optimal measurement within that scheme. Our variational approach can be applied following two different strategies: *in situ* [42,44,45], i.e., optimizing the PQC directly on the quantum hardware, or *in silicon*, i.e., simulating the PQC on a classical computer and then running the quantum hardware with the optimal parameters [43,46]. Codes to reproduce the results of this manuscript are available in [47].

II. ALGORITHM

Let us initially restrict ourselves to the noiseless case. Our VQA can be divided into two steps: preparation and measurement, as sketched in Fig. 1(a) (more details can be found in Appendix A). In the preparation stage, a PQC described by a unitary operator $U_P(\boldsymbol{\theta})$ is applied to two cavity modes. The initial state of each cavity is a coherent state with mean-photon number $|\alpha|^2 = N/2$ [48], such that the mean number of photons summing both arms is N [49]. The resulting state $|\psi_P(\boldsymbol{\theta})\rangle$ is then sent through a MZI consisting of a symmetric beam splitter followed by the encoding of a phase difference φ between the two modes and by another symmetric beam splitter, resulting in a state $|\psi_E(\boldsymbol{\theta}, \varphi)\rangle$. To optimize the preparation of probe states, one needs to maximize the QFI $\mathcal{F}_Q$, thus setting the cost function to $C_P(\boldsymbol{\theta}, \varphi) = -\mathcal{F}_Q$. Then, this quantity is fed to the classical optimizer, which in turn updates the parameters $\boldsymbol{\theta}$. The lower bound on the estimation error on φ is given by the quantum Cramér-Rao bound $(\Delta\varphi)^2 \geqslant \mathcal{F}_Q^{-1}$ [11]. The closer $\mathcal{F}_Q^{-1}$ is to the HL, the larger the metrological potential obtained with the PQC.

To calculate the QFI, we use the approximation introduced in Ref. [38]; see Appendix A for more details. This requires evaluating the fidelity between the states $|\psi_E(\boldsymbol{\theta}, \varphi)\rangle$ and $|\psi_E(\boldsymbol{\theta}, \varphi + \delta)\rangle$, where $\delta \to 0$ is a small phase difference. In principle, this demands a number of measurements as well as an amount of computation growing exponentially with the system size [50]. In Appendix C we review some of the most promising techniques to measure the QFI—or, equivalently, the fidelity between two quantum states—aimed at alleviating this problem. Besides, the small size of the platform considered in our manuscript (hosting only two photonic modes, which implies a Hilbert space dimension scaling quadratically with N) will further reduce the complexity of fidelity measurements.

Since the QFI is maximized irrespective of the measurement scheme, in the second step of the protocol we assess the best way to extract the information within a specific measurement type. In particular, we first apply a unitary $U_M(\boldsymbol{\mu})$ to the output state $|\psi_E(\boldsymbol{\theta}_{opt}, \varphi)\rangle$ resulting from the previous optimization and then we consider a measurement in the photon-number basis. The role of the unitary, which we label as measurement PQC, is to enable the algorithm to find the best possible combination of modes before measuring. The optimal parameters $\boldsymbol{\mu}_{opt}$ are found by maximizing the CFI $\mathcal{F}_C$, which we use as the new cost function of our algorithm $C_M(\boldsymbol{\theta}_{opt}, \varphi, \boldsymbol{\mu}) = -\mathcal{F}_C$. To compute the CFI, we construct the density matrix $\rho_M(\boldsymbol{\theta}_{opt}, \varphi, \boldsymbol{\mu}) = |\psi_M(\boldsymbol{\theta}_{opt}, \varphi, \boldsymbol{\mu})\rangle\langle\psi_M(\boldsymbol{\theta}_{opt}, \varphi, \boldsymbol{\mu})|$, where $|\psi_M(\boldsymbol{\theta}_{opt}, \varphi, \boldsymbol{\mu})\rangle = U_M(\boldsymbol{\mu})|\psi_E(\boldsymbol{\theta}_{opt}, \varphi)\rangle$. With this expression and its derivative $\partial\rho_M(\boldsymbol{\theta}_{opt}, \varphi, \boldsymbol{\mu})/\partial\varphi$, we calculate the CFI (see Appendix A) and optimize it. An optimal measurement should give $\mathcal{F}_C = \mathcal{F}_Q$; such hierarchy is again summarized by the quantum Cramér-Rao bound $(\Delta\varphi)^2 \geqslant \mathcal{F}_C^{-1} \geqslant \mathcal{F}_Q^{-1}$ [11].

III. PHYSICAL PLATFORMS AND ANSÄTZE

A crucial element of VQAs is the chosen PQC, since it determines the solution space that the algorithm can explore. In our case, the PQC will be defined by the two architectures represented in Figs. 1(b)–1(e). Their common ingredients are

two coupled single-mode cavities described by bosonic annihilation (creation) operators $a_{1,2}^{(\dagger)}$, whose coupling Hamiltonian reads $H_{\rm t} = J(a_2^\dagger a_1 + a_1^\dagger a_2)$, where J is the tunneling rate. The difference stems in the source of nonlinearity.

On the one hand [see Figs. 1(b) and 1(c)], we consider a nonlinearity coming from the coupling to a two-level emitter, like in cavity QED setups [44,51–53]. This platform enables encoding three different variational parameters per layer, namely, J, the emitter-cavity detuning Δ, and the coupling strength g, whose corresponding Hamiltonians read $H_{\rm e}^{(i)} = \Delta\sigma_i^\dagger\sigma_i$ and $H_{\rm int}^{(i)} = g(\sigma_i^\dagger a_i + \sigma_i a_i^\dagger)$, respectively. Here, $\sigma_i = |g\rangle\langle e|$ takes the emitter i from its excited state $|e\rangle$ to its ground state $|g\rangle$. In this case, the unitary describing the PQC can be written as

$$U_{\rm P,M}^{(\rm emit)} = \prod_{j=1}^{d} U_{\rm int}^{(2,j)} U_{\rm int}^{(1,j)} U_{\rm e}^{(2,j)} U_{\rm e}^{(1,j)} U_{\rm t}^{(j)}. \tag{1}$$

Above, d is the number of layers of the PQC, $U_{\rm t}^{(j)} = e^{-iT_j^{(J)}H_{\rm t}}$, $U_{\rm e}^{(i,j)} = e^{-iT_j^{(\Delta)}H_{\rm e}^{(i)}}$, and $U_{\rm int}^{(i,j)} = e^{-iT_j^{(g)}H_{\rm int}^{(i)}}$, where $T_j^{(J,\Delta,g)}$ is the physical time in which each term is applied. $\boldsymbol{\theta}, \boldsymbol{\mu} = \{\tilde{J}_1, \tilde{\Delta}_1, \tilde{g}_1, \ldots, \tilde{J}_d, \tilde{\Delta}_d, \tilde{g}_d\}$ are the variational parameters, each given by $\tilde{J}_j = J_j T_j^{(J)}$, $\tilde{\Delta}_j = \Delta_j T_j^{(\Delta)}$, and $\tilde{g}_j = g_j T_j^{(g)}$. The number of gates is $N_{\rm gates} = 3d$.

On the other hand [see Figs. 1(d) and 1(e)], we consider the Kerr-type Hamiltonian $H_{\rm Kerr}^{(i)} = U/2 \times a_i^\dagger a_i(a_i^\dagger a_i - 1)$ arising, for example, from $\chi^{(3)}$ nonlinearities in nonlinear crystals [54]. With these interactions, we can write the *Ansatz* of the Kerr nonlinear circuit as follows:

$$U_{\rm P,M}^{(\rm Kerr)} = \prod_{j=1}^{d} U_{\rm Kerr}^{(2,j)} U_{\rm Kerr}^{(1,j)} U_{\rm t}^{(j)}, \tag{2}$$

where $\boldsymbol{\theta}, \boldsymbol{\mu} = \{\tilde{J}_1, \tilde{U}_1, \ldots, \tilde{J}_d, \tilde{U}_d\}$ are the variational parameters (two per layer), each given by $\tilde{J}_j = J_j T_j^{(J)}$ and $\tilde{U}_j = U_j T_j^{(U)}$. $T_j^{(J,U)}$ is the physical time in which each term is applied. The number of gates is $N_{\rm gates} = 2d$. Compared to earlier works [43], we use the Kerr nonlinearity as a variational parameter to check if it can provide an advantage over fixed U *Ansätze*. A discussion on the physical realization of tunable optical nonlinearities is included in Appendix D, both for the Kerr nonlinearity and the photon-emitter interaction.

Ideally, we would like the VQA to use an *Ansatz* with as few gates as possible. The reason is that, e.g., if we assume a constant error per gate ε, the overall fidelity of state generation after performing $N_{\rm gates}$ will be $(1-\varepsilon)^{N_{\rm gates}}$.

IV. NOISELESS RESULTS

In Fig. 2 we show the convergence of our algorithm for the QFI with respect to the number of layers d (and gates, $N_{\rm gates}$) of the preparation PQC for the emitters [panel (a)] and the Kerr nonlinearity [panel (b)]*Ansätze*. Both panels show $\mathcal{F}_{\rm Q}^{-1}$ as d is varied for different mean number of photons N ranging from $N = 10$ to $N = 50$. For both *Ansätze* convergence is rapidly obtained with only two layers, making our protocol extraordinarily efficient in terms of circuit depth. What is more important, the value of d at which convergence is attained does not depend on N, at least for the range of N studied.

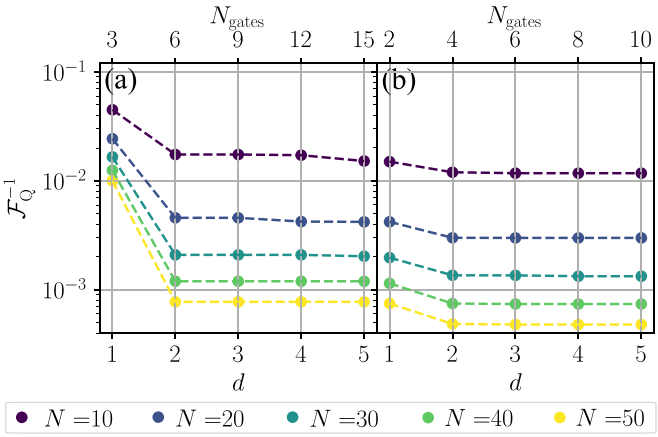

FIG. 2. Scaling of the inverse of the QFI $\mathcal{F}_{\rm Q}^{-1}$ as a function of the number of layers d (and gates, $N_{\rm gates}$) of the PQC, for different values of the mean number of photons N. (a) Emitters *Ansatz*. (b) Kerr *Ansatz*.

This is in stark contrast with state-of-art protocols [18,20] in which $N_{\rm gates} \sim N$, and thus the fidelity decays exponentially the number of photons.

Once we guarantee the convergence of the preparation step, we study whether optimal probe states and optimal measurements can be obtained with our protocol. Our results are shown in Fig. 3. In panel (a) we plot the estimation error $(\Delta\varphi)^2$ as a function of the mean number of photons N in the VQA protocol for a circuit depth $d = 5$ [55]. The values of $\mathcal{F}_{\rm Q}^{-1}$ obtained with both *Ansätze* are smaller than $(\Delta\varphi)^2$ for TFS with $N/2$ Fock states in each arm [12]. While the optimal states produced by the Kerr *Ansatz* saturate the HL for small N and remain very close to it as N grows, those generated by the emitters *Ansatz* start approaching the HL at $N \gtrsim 20$. A linear fit reveals that our results follow a scaling $\mathcal{F}_{\rm Q}^{-1} \sim 1/N^\beta$

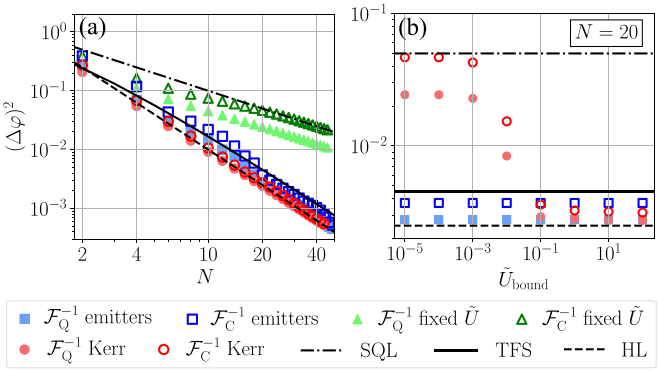

FIG. 3. Estimation error $(\Delta\varphi)^2$ in the noiseless scenario. Panel (a) shows our results as a function of the mean number of photons N. In panel (b), we address the effect of a bound in the Kerr nonlinearity strength $\tilde{U}_{\rm bound}$ for a mean number of photons $N = 20$. In both panels, blue squares, red circles, and green triangles correspond to the results of the emitters *Ansatz*, the Kerr *Ansatz* with unrestricted $\tilde{U}$, and the Kerr *Ansatz* with fixed $\tilde{U} = 2\pi$, respectively: filled (void) markers are the inverse of the QFI (CFI) $\mathcal{F}_{\rm Q(C)}^{-1}$ in the two cases. Dashed-dotted/solid/dashed lines signal the SQL/TFS/HL scaling. In both panels, we employed a circuit depth $d = 5$.

very similar to that of the HL: $\beta = 2.0$ for the emitters *Ansatz* and $\beta = 1.95$ for the Kerr one. More details on the nature of the states prepared by our VQA, as well as a comparison with NOON states and TFS, are provided in Appendix F. Regarding $\mathcal{F}_{\rm C}^{-1}$, the results of the Kerr *Ansatz* are very close to the respective values of $\mathcal{F}_{\rm Q}^{-1}$. In the case of the emitters *Ansatz*, the CFI closely follows the QFI, although complete saturation is not attained. In any case, both *Ansätze* are able to prepare almost optimal measurements. We benchmarked these results with those of the Kerr *Ansatz* featuring a fixed value of the nonlinearity variational parameter $\tilde{U} = 2\pi$, as in Ref. [43]. In this case, $\mathcal{F}_{\rm Q,C}^{-1}$ tend to the classical $1/N$ scaling, signaling that the tunability of the nonlinearity strength is a crucial factor to obtain metrological advantage.

To implement our protocol in an experiment, one needs to verify that the optimal values of the variational parameters are within the reach of state-of-the-art optical platforms. In particular, very strong optical nonlinearities may not be physically realizable. In Appendix G, we show that for our tunable nonlinearity *Ansätze* the maximum values of $\tilde{g}$ and $\tilde{U}$ required are of the order of 1. Since $T_i^{(J,\Delta,g,U)}$ are limited by the coherence time κ^{-1}, g and U must be smaller than the typical decoherence rates in the systems. Such coherence times are within the reach of certain cavity-QED platforms in both the microwave and optical regimes [56–60]. However, in Kerr optical cavities the current record is held by polaritonic systems with only $U/\kappa \sim 10^{-2}$ [61,62], while microwave resonators reach $U/\kappa \sim 10^{2}$ [63–65]. This limitation motivated us to study the effect of restricted Kerr nonlinearities in the optimization. For that, we introduce a bound $\tilde{U} \in [-\tilde{U}_{\rm bound}, \tilde{U}_{\rm bound}]$ in the range of parameters that the optimizer can explore and study the dependence of $\mathcal{F}_{\rm Q}$ and $\mathcal{F}_{\rm C}$ on $\tilde{U}_{\rm bound}$. The results are displayed in Fig. 3(b) for fixed $N = 20$, showing two distinct behaviors for $\tilde{U}_{\rm bound} \lesssim 10^{-3}$ and $\tilde{U}_{\rm bound} \gtrsim 10^{-1}$ with a continuous crossover in between. In the former regime, which is the one realistically achievable with state-of-the-art optical platforms, the bound prevents the optimizer from exploring the region of the Hilbert space where the minimum of the cost function lies and the resulting values of QFI and CFI are the ones that would be obtained using coherent states at the input of the Mach-Zehnder interferometer (see Appendix H). However, above a critical value of $\tilde{U}_{\rm bound}$, the optimizer finds a very similar solution to that obtained using the emitters *Ansatz*. In Appendix I, we study the dependence of this critical $\tilde{U}_{\rm bound}$ on different mean-photon numbers, showing that it does not depend strongly on N for the photon numbers we can explore.

V. EFFECT OF NOISE

As a last step, we extend the previous study to a more realistic situation including noise in the quantum channels. Formally, we do it by constructing the density matrix $\rho_{\rm E}(\boldsymbol{\theta}_{\rm opt}, \varphi) = |\psi_{\rm E}(\boldsymbol{\theta}_{\rm opt}, \varphi)\rangle\langle\psi_{\rm E}(\boldsymbol{\theta}_{\rm opt}, \varphi)|$ after the MZI and letting it experience a nonunitary evolution according to the Lindblad master equation $\dot{\rho}_{\rm E} = \kappa \sum_{i=1}^{2} [L_i \rho_{\rm E}(t) L_i^\dagger - \frac{1}{2}\{L_i^\dagger L_i, \rho_{\rm E}(t)\}]$, where $\{L_i\}$ is the set of jump operators describing the noise channel and κ is the loss rate, which for simplicity we assume to be equal for all channels. As a further simplification, we include noise of two types only on the photonic degrees of freedom: amplitude (i.e., photon loss) and phase damping (i.e., decoherence) [66]. For the former, the set of jump operators is $\{a_1, a_2\}$, resulting in a decay of the photonic population in both modes. In the latter, the set of jump operators is $\{a_1^\dagger a_1, a_2^\dagger a_2\}$. This in turn preserves the diagonal elements of the density matrix (i.e., the occupation probabilities) while producing a decay in its off-diagonal elements (i.e., erasing the coherences).

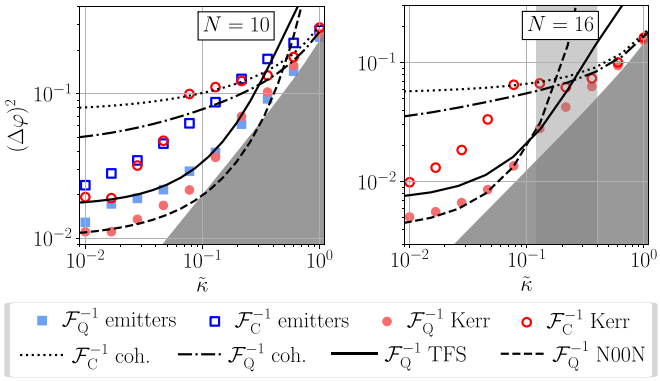

FIG. 4. Estimation error $(\Delta\varphi)^2$ as a function of the dimensionless noise parameter $\tilde{\kappa}$ for mean photon numbers $N = 10$ [panel (a)] and $N = 16$ [panel (b)]. Blue squares (red circles) correspond to the results of the emitters (Kerr) *Ansatz*: filled (void) markers are the inverse of the quantum (classical) Fisher information $\mathcal{F}_{\rm Q(C)}^{-1}$ in the two cases. Dashed-dotted/solid/dashed lines signal the values of $\mathcal{F}_{\rm Q}^{-1}$ obtained for coherent states/TFS/NOON states without preparation PQC. The dotted line corresponds to $\mathcal{F}_{\rm C}^{-1}$ for coherent states without measurement PQC. In the light gray shaded area of panel (b) the optimal states attain values of $\Delta\varphi$ which are sizeably smaller than those of TFS. The dark gray shaded area is beyond the asymptotic bound for dephasing noise [67]. In both panels, we employed the circuit depth $d = 5$.

Figure 4 shows the results of our algorithm in the presence of both noise channels for a circuit depth $d = 5$ and fixed photon numbers $N = 10$ [panel (a)] and $N = 16$ [panel (b)] as a function of the dimensionless noise factor $\tilde{\kappa} = \kappa T_\kappa$, where T_κ is the typical noise timescale. For $N = 16$ only the results for the Kerr *Ansatz* are shown, as the calculation for the emitters one does not reach such value of N due to the numerical overhead introduced by the emitters degrees of freedom. We benchmark the optimal values obtained with our VQA with those given by coherent states with $\alpha = \sqrt{N/2}$, TFS $|N/2\rangle \otimes |N/2\rangle$, and NOON states $(|N, 0\rangle + |0, N\rangle)/\sqrt{2}$ alone without the preparation and measurement PQCs. In general, as $\tilde{\kappa}$ increases, the values of $\mathcal{F}_{\rm Q}^{-1}$ obtained with both the emitters and the Kerr *Ansätze* are lifted upwards, attaining values similar to those of NOON and TFS up to the value of $\tilde{\kappa}$ where these states surpass the coherent ones. On the contrary, for larger values of $\tilde{\kappa}$ the states generated by our VQA maintain a metrological advantage over coherent states. This improvement becomes larger with growing N, as can be seen in panel (b), which features a range of $\tilde{\kappa}$ (shaded in light gray) in which the variationally computed value of $\mathcal{F}_{\rm Q}^{-1}$ is sizeably smaller than that of TFS, which are considered noise-robust states [11,68]. This places the states generated by our protocol amongst the most noise-resilient ones. As $\tilde{\kappa}$ grows such improvement diminishes, as it is expected for all generation protocols. The dark gray shaded area represents the region beyond the

asymptotic bound (for large N) in the presence of dephasing noise [67]. For $\tilde{\kappa} \gtrsim 10^{-1}$ the results of our optimal states are close to such a bound. As for the CFI, it turns out to be more susceptible to noise and even for small values of $\tilde{\kappa}$ it deviates significantly from the corresponding QFI, reaching the CFI of coherent states for smaller $\tilde{\kappa}$. This implies that photon number measurements are not a good choice in a noisy situation.

VI. CONCLUSIONS AND OUTLOOK

Summing up, using a variational approach, we propose a method to generate metrologically relevant photonic states which offer an exponential advantage over standard deterministic protocols when gate errors are considered. By comparing the performance of both Kerr and emitter nonlinearities, we predict that the emitter *Ansatz* will perform better in platforms with limited Kerr nonlinearities. We also showed that the tunable character of the nonlinearity is essential to reach a Heisenberg scaling in the estimation error. Interestingly, our method is able to find states which provide a metrological advantage in the presence of moderate values of noise beyond other noise-resilient states considered in the literature, such as twin-Fock states. In future works, we plan to extend our algorithm beyond the two-mode scenario in order to study multiparameter estimation [34], as well as to apply it to other relevant problems in metrology such as electric field estimation [69].

ACKNOWLEDGMENTS

The authors acknowledge support from the Proyecto Sinérgico CAM 2020 Y2020/TCS-6545 (NanoQuCo-CM), the CSIC Research Platform on Quantum Technologies PTI-001 and from Spanish Projects No. PID2021-127968NB-I00 and No. TED2021-130552B-C22 funded by MCIN/AEI/10.13039/501100011033/FEDER, UE and MCIN/AEI/10.13039/501100011033, respectively. A.M.H. acknowledges support from Fundación General CSIC's ComFuturo program, which has received funding from the European Union's Horizon 2020 research and innovation program under the Marie Skłodowska-Curie Grant Agreement No. 101034263. C.T. acknowledges support from Comunidad de Madrid (PIPF-2022/TEC-25625) and also from Fundación Humanismo y Ciencia. A.G.T. also acknowledges support from a 2022 Leonardo Grant for Researchers and Cultural Creators, and BBVA Foundation. The authors also acknowledge Centro de Supercomputación de Galicia (CESGA) who provided access to the supercomputer FinisTerrae for performing numerical simulations. The authors thank M. Perarnau-Llobet, J. J. García-Ripoll, and G. Giedke for insightful discussions.

APPENDIX A: DESCRIPTION OF THE VARIATIONAL QUANTUM ALGORITHM

In this Appendix we describe in more detail the VQA proposed in our work. In general, we envision a quantum system featuring two photonic modes. Each of them initially hosts a coherent state

$$|\alpha\rangle = e^{-|\alpha|^2/2} \sum_{n=0}^{\infty} \frac{\alpha^n}{\sqrt{n!}} |n\rangle, \tag{A1}$$

with a mean-photon number $|\alpha|^2 = N/2$. In practice, the infinite sum above is truncated at N, ensuring that the maximum number of photons in the system is $2N$. The initial state in the Kerr *Ansatz* (which does not include emitters) therefore is $|\psi_0\rangle = |\alpha\rangle_1 \otimes |\alpha\rangle_2$, where the subscripts 1,2 refer to the photonic mode. In the emitters *Ansatz*, we assume that the two-level emitters are initially in their ground state $|g\rangle$, thus giving an initial state $|\psi_0\rangle = |\alpha\rangle_1 \otimes |\alpha\rangle_2 \otimes |g\rangle_1 \otimes |g\rangle_2$. The subscripts in the state of the emitters refer to the photonic mode to which they are coupled.

In the preparation stage, a parametrized quantum circuit (PQC) described by a unitary $U_{\rm P}(\boldsymbol{\theta})$ is applied to the initial state. As explained in the main text, the applied unitary depends on the ansatz. The resulting state is $|\psi_{\rm P}(\boldsymbol{\theta})\rangle = U_{\rm P}(\boldsymbol{\theta})|\psi_0\rangle$.

Such state is then sent through a Mach-Zehnder interferometer (MZI) consisting of a symmetric beam splitter (described by a unitary $U_{\rm BS} = \exp[-i(a_2^\dagger a_1 + a_1^\dagger a_2)\pi/4]$) followed by the encoding of a phase difference φ between the two modes (given by a unitary $U_{\rm E}(\varphi) = \exp[i\varphi(a_1^\dagger a_1 - a_2^\dagger a_2)/2]$) and another symmetric beam splitter, resulting in a state $|\psi_{\rm E}(\boldsymbol{\theta}, \varphi)\rangle = U_{\rm BS} U_{\rm E}(\varphi) U_{\rm BS} |\psi_{\rm P}(\boldsymbol{\theta})\rangle$. A second copy of $|\psi_{\rm P}(\boldsymbol{\theta})\rangle$ is also sent through the MZI, but in this case the encoded phase is $\varphi + \delta$, where $\delta \ll 1$ is a small parameter. This allows us to calculate the QFI later on. Without loss of generality, in all our calculations we took $\varphi = \pi/3$ and $\delta = 10^{-2}$.

In order to account for noise in the preparation and encoding stages, we need to construct the density matrices $\rho_{\rm E}(\boldsymbol{\theta}, \varphi) = |\psi_{\rm E}(\boldsymbol{\theta}, \varphi)\rangle\langle\psi_{\rm E}(\boldsymbol{\theta}, \varphi)|$ and $\rho_{\rm E}(\boldsymbol{\theta}, \varphi + \delta) = |\psi_{\rm E}(\boldsymbol{\theta}, \varphi + \delta)\rangle\langle\psi_{\rm E}(\boldsymbol{\theta}, \varphi + \delta)|$, which experience a nonunitary evolution according to a Lindblad master equation. We consider two noise channels: amplitude damping and phase damping, as explained in the main text, each featuring a loss rate κ. However, working with density matrices is computationally expensive since it requires squaring the dimension of the Hilbert space. Therefore, in practice, when we have $\kappa > 0$ we work with vectorized density matrices following the Choi-Jamiolkowski isomorphism [70], but in the noiseless case ($\kappa = 0$) we avoid it and deal directly with state vectors.

In the noisy case the resulting state is given by $\rho_{\rm E}(\boldsymbol{\theta}, \varphi, \kappa) = e^{\mathcal{L}_{pd} T_\kappa} e^{\mathcal{L}_{ad} T_\kappa} \rho_{\rm E}(\boldsymbol{\theta}, \varphi) e^{\mathcal{L}_{ad}^\dagger T_\kappa} e^{\mathcal{L}_{pd}^\dagger T_\kappa}$, where T_κ is a typical noise timescale which for simplicity we assume equal for both noise channels and $\mathcal{L}_{\rm ad,pd}$ are the Lindbladian superoperators for amplitude damping and phase damping given by

$$\mathcal{L}_{\rm ad,pd} = \kappa \sum_{i=1}^{2} \left[L_i^{\rm (ad,pd)} \rho(t) L_i^{\rm (ad,pd)^\dagger} - \frac{1}{2} \left\{ L_i^{\rm (ad,pd)^\dagger} L_i^{\rm (ad,pd)}, \rho(t) \right\} \right]. \tag{A2}$$

The sum above is over the set of jump operators belonging to the two noise channels, given by $\{L^{\rm (ad)}\} = \{a_1, a_2\}$ and $\{L^{\rm (pd)}\} = \{a_1^\dagger a_1, a_2^\dagger a_2\}$, where a_i is the annihilation operator acting on the photonic mode i.

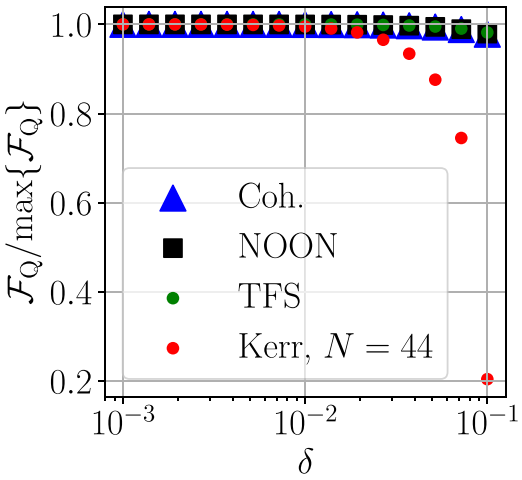

FIG. 5. QFI $\mathcal{F}_Q$ normalized in units of its converged value $\max\{\mathcal{F}_Q\}$ for coherent states, NOON states, TFS, and an optimal Kerr state with mean photon number $N = 44$ obtained with our VQA as a function of δ.

The QFI $\mathcal{F}_Q$ is then calculated following the approximate formula [38]

$$\mathcal{F}_Q = 8\frac{1 - F(\varphi, \varphi + \delta)}{\delta^2}, \tag{A3}$$

where $F(\varphi, \varphi + \delta)$ is the fidelity between the states in which the phases φ and $\varphi + \delta$ were encoded. This is calculated as

$$F(\varphi, \varphi + \delta) = |\langle\psi_E(\boldsymbol{\theta}, \varphi)|\psi_E(\boldsymbol{\theta}, \varphi + \delta)\rangle|, \tag{A4}$$

$$F(\varphi, \varphi + \delta) = \sqrt{\sqrt{\rho_E(\boldsymbol{\theta}, \varphi, \kappa)}\rho_E(\boldsymbol{\theta}, \varphi + \delta, \kappa)\sqrt{\rho_E(\boldsymbol{\theta}, \varphi, \kappa)}} \tag{A5}$$

in the noiseless and in the noisy case [71], respectively. Remember that Eq. (A3) is valid in the limit $\delta \to 0$.

In a realistic implementation, this procedure can be implemented by considering two different state evolutions in the MZI: (i) applying opposite phase shifts $\pm\delta/2$ in the two channels of the MZI and (ii) leaving the two channels unperturbed, without applying any phase shift. The resulting states are then used to calculate the QFI according to Eq. (A3). Therefore, δ plays the role of the parameter to be estimated. While in our calculations we considered a phase shift $\varphi = \pi/3$, that choice is arbitrary and considering $\varphi = 0$ does not change the results, because the value of the QFI does not depend on the choice of φ [37]. We give more information on how to experimentally estimate the QFI and the fidelity in Appendix C.

Also, to make sure that our results are converged, we plotted the QFI attained by several states as a function of δ (see Fig. 5). From such results it is evident that $\delta = 10^{-2}$ is a safe choice.

To maximize the QFI we choose a cost function $C_P(\boldsymbol{\theta}, \varphi, \kappa) = -\mathcal{F}_Q$. This quantity is fed to the classical optimizer, which in turn updates the parameters $\boldsymbol{\theta}$. We initialize the preparation PQC close to the identity matrix (i.e., $\boldsymbol{\theta}$ finite but close to 0) and employ COBYLA [72] as the classical optimizer, since it was the one giving the best results in a reasonable convergence time. When the optimization converges, we get the output state evaluated at the optimal parameters $\rho_E(\boldsymbol{\theta}_{opt}, \varphi, \kappa)$ in the noisy case and $|\psi_E(\boldsymbol{\theta}_{opt}, \varphi)\rangle$ in the noiseless one.

Such state is sent through the measurement PQC, which is characterized by a unitary $U_M(\boldsymbol{\mu})$, resulting in a state described by $\rho_M(\boldsymbol{\theta}_{opt}, \varphi, \kappa, \boldsymbol{\mu}) = U_M(\boldsymbol{\mu})\rho_E(\boldsymbol{\theta}_{opt}, \varphi, \kappa)U_M(\boldsymbol{\mu})^\dagger$ in the noisy case and $|\psi_M(\boldsymbol{\theta}_{opt}, \varphi, \boldsymbol{\mu})\rangle = U_M(\boldsymbol{\mu})|\psi_E(\boldsymbol{\theta}_{opt}, \varphi)\rangle$ in the noiseless one.

At this point, we construct the density matrix for the noiseless case as $\rho_M(\boldsymbol{\theta}_{opt}, \varphi, \kappa = 0, \boldsymbol{\mu}) = |\psi_M(\boldsymbol{\theta}_{opt}, \varphi, \boldsymbol{\mu})\rangle\langle\psi_M(\boldsymbol{\theta}_{opt}, \varphi, \boldsymbol{\mu})|$. Then, the derivative $\partial\rho_M(\boldsymbol{\theta}_{opt}, \varphi, \kappa, \boldsymbol{\mu})/\partial\varphi$ is computed by means of the chain rule. The density matrix and its derivative are used to calculate the CFI,

$$\mathcal{F}_C = \sum_n \frac{1}{\rho_{M,nn}(\boldsymbol{\theta}_{opt}, \varphi, \kappa, \boldsymbol{\mu})}\left(\frac{\partial\rho_{M,nn}(\boldsymbol{\theta}_{opt}, \varphi, \kappa, \boldsymbol{\mu})}{\partial\varphi}\right)^2, \tag{A6}$$

where the sum is carried over the diagonal elements n, n. To maximize the classical Fisher information (CFI), we set a cost function $C_M(\boldsymbol{\theta}_{opt}, \varphi, \kappa, \boldsymbol{\mu}) = -\mathcal{F}_C$. This value is fed to the classical optimizer, which in turn returns the optimal measurement parameters $\boldsymbol{\mu}_{opt}$. As for the preparation PQC, the measurement PQC is initialized close to the identity matrix (i.e., $\boldsymbol{\mu}$ finite but close to 0), and we employed COBYLA as the classical optimizer.

As one can see, the two optimizations for the QFI and the CFI are carried separately in our VQA.

APPENDIX B: STARTING FROM SQUEEZED COHERENT STATES

In this Appendix we perform an analog calculation to that shown in the main text but employing squeezed coherent states [48] as initial states:

$$|\alpha, r\rangle = \frac{1}{\sqrt{\cosh r}}\exp\left(-\frac{1}{2}|\alpha|^2 - \frac{1}{2}\alpha^{*2}\tanh r\right) \times \sum_{n=0}^{\infty}\frac{\left(\frac{1}{2}\tanh r\right)^{n/2}}{\sqrt{n!}}H_n\left(\frac{\gamma}{\sqrt{\sinh(2r)}}\right)|n\rangle, \tag{B1}$$

where $\gamma = \alpha\cosh r + \alpha^*\sinh r$ and H_n is the Hermite polynomial of grade n. The initial state is therefore $|\psi_0\rangle = |\alpha, r\rangle_1 \otimes |\alpha, r\rangle_2$ for the Kerr *Ansatz* and $|\psi_0\rangle = |\alpha, r\rangle_1 \otimes |\alpha, r\rangle_2 \otimes |g\rangle_1 \otimes |g\rangle_2$ for the emitters one. We choose $\alpha = \sqrt{N/2}$ as in the coherent states case and r (the squeezing parameter) to be 10 dB, which is within the reach of state-of-the-art optical technology [73]. In practice, the infinite sum in Eq. (B1) is truncated at N, ensuring that the maximum number of photons in the system is $2N$. Using squeezed coherent states instead of coherent ones as initial states could be of help since the algorithm already starts from nonclassical states, making it easier to obtain a quantum advantage.

Figure 6(a) shows the estimation error $(\Delta\varphi)^2$ obtained from maximizing the QFI and the CFI using our VQA as a function of N and for a circuit depth $d = 5$. As one can see, the difference between employing squeezed or coherent states [Fig. 3(a) of the main text] as initial states is negligible: in both cases, the optimizer is able to find almost identical values for the QFI and the CFI. This is true for both *Ansätze*.

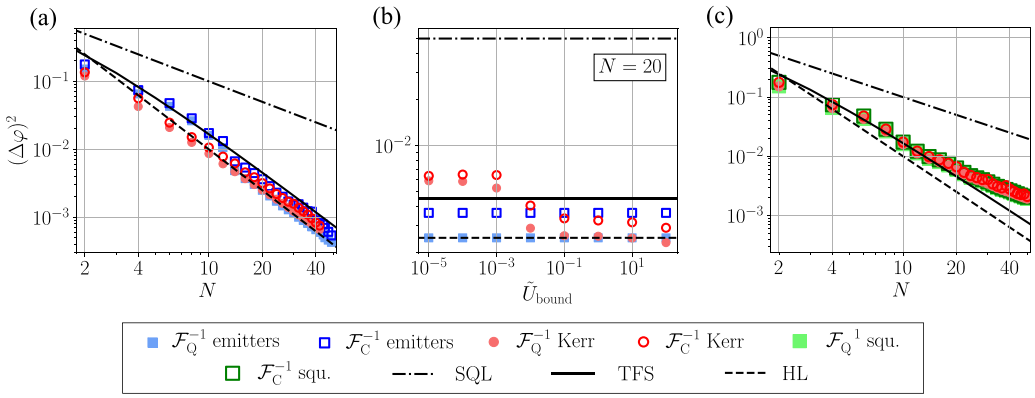

FIG. 6. Estimation error $(\Delta\varphi)^2$ in the noiseless scenario starting from squeezed coherent states with $\alpha = \sqrt{N/2}$ and a squeezing factor of 10 dB. Panel (a) shows our results as a function of the mean number of photons N. In panel (b), we address the effect of a bound in the Kerr nonlinearity strength $\tilde{U}_{\text{bound}}$ for a mean number of photons $N = 20$. Panel (c) compares the results of the Kerr *Ansatz* with $\tilde{U}_{\text{bound}} = 10^{-4}$ with those obtained removing the preparation and measurement PQCs. In the three panels, blue squares/red circles/green squares correspond to the results of the emitters *Ansatz*/Kerr *Ansatz*/squeezed states without preparation and measurement PQCs: filled (void) markers are the inverse of the QFI (CFI) $\mathcal{F}_{\text{Q(C)}}^{-1}$ in the three cases. Dashed-dotted/solid/dashed lines signal the SQL/TFS/HL scaling. All calculations were made employing PQCs with depth $d = 5$.

To further explore whether squeezed states provide any advantage over coherent ones, we also plot the values of $\mathcal{F}_{\text{Q,C}}^{-1}$ obtained by both *Ansätze* as a function of a bound in the Kerr nonlinearity variational parameter $\tilde{U}_{\text{bound}}$. We fix the mean number of photons at $N = 20$. Nevertheless, we obtain a very similar behavior to that of coherent states [shown in Fig. 3(b) of the main text], with a threshold located at $\tilde{U}_{\text{bound}} = 10^{-2}$ separating below a regime where the Kerr *Ansatz* results lie above those obtained with the emitters one and above one where the results of both *Ansätze* are very similar. Therefore, optical platforms only able to reach $U/\kappa \sim 10^{-2}$ at most [61] will suffer from the same expressibility problems employing either coherent or squeezed states. Overall, the results of Figs. 6(a) and 6(b) discard the possibility of obtaining better results using squeezed coherent states.

Finally, to understand better what is happening below the Kerr nonlinearity bound threshold, we plot in Fig. 6(c) the values of $\mathcal{F}_{\text{Q,C}}^{-1}$ obtained with the Kerr *Ansatz* with a bound $\tilde{U}_{\text{bound}} = 10^{-4}$ as a function of N. Here we also plot the results for the inverse of the QFI and the CFI using squeezed coherent states with $\alpha = \sqrt{N/2}$ and a squeezing factor of 10 dB, i.e., removing the preparation and measurement PQCs (or equivalently setting $\boldsymbol{\theta} = \boldsymbol{\mu} = 0$). The results are identical in both cases, showing that the bound Kerr *Ansatz* is not able to surpass the results of squeezed states alone due to the small value of $\tilde{U}_{\text{bound}}$ preventing the optimizer to explore a larger region of the Hilbert space. In any case, these results are better than those obtained with coherent states alone, as is shown in Appendix H, since the former are already nonclassical. Note that, while squeezed states saturate the TFS scaling at small values of N, for $N \gtrsim 20$ they deviate and start following a classical $1/N$ scaling.

APPENDIX C: MEASURING THE QFI

In this Appendix, we provide more insight on the different techniques proposed to measure the QFI. In our calculations, we compute the QFI by means of Eq. (A3). This procedure consists of evaluating the evolution of the quantum state through the MZI subjected to two different phase differences: φ and $\varphi + \delta$. Such an approximation is valid in the limit of small δ. In order to obtain the QFI, one must evaluate the fidelity between the states generated by the two different evolutions. We choose to calculate the QFI this way because the alternatives (which involve either the eigendecomposition of the density matrix or evaluating the symmetric logarithmic derivative [37,74]) are computationally more expensive. Besides, in our manuscript we are dealing with a two-mode photonic system (with each of the modes coupled to a two-level emitter in the case of the emitters *Ansatz*) in which the dimension of the total Hilbert space scales quadratically with respect to the mean number of photons present in the system N. We therefore expect measurements of the QFI (or, equivalently, the fidelity) to be simpler than in the most general case, in which the complexity scales exponentially with N. Even in that case, there exist a number of strategies aimed at mitigating the cost of brute-force full quantum state tomography to access the spectrum of eigenvalues and eigenstates of the density matrices. Here we mention the most promising ones, although the list is not complete.

(1) In the case of states that are well approximated by matrix product states (MPS) [50] proposed two schemes for efficient quantum state tomography which only require a linear amount (on the system size) of local observables as well as polynomial classical postprocessing of the data. Efficient quantum state tomography can be also obtained by harnessing conditional generative adversarial neural networks [75], which leads to orders of magnitude fewer iterative steps than full quantum state tomography.

(2) An alternative approach to measure the fidelity between two quantum states is given by randomized measurements [76]. This strategy consists of repeatedly preparing and measuring a quantum state in a randomly chosen basis. A classical computer then processes the measurement outcome to estimate the desired property. In particular, a fidelity measurement will still feature an exponential complexity on the

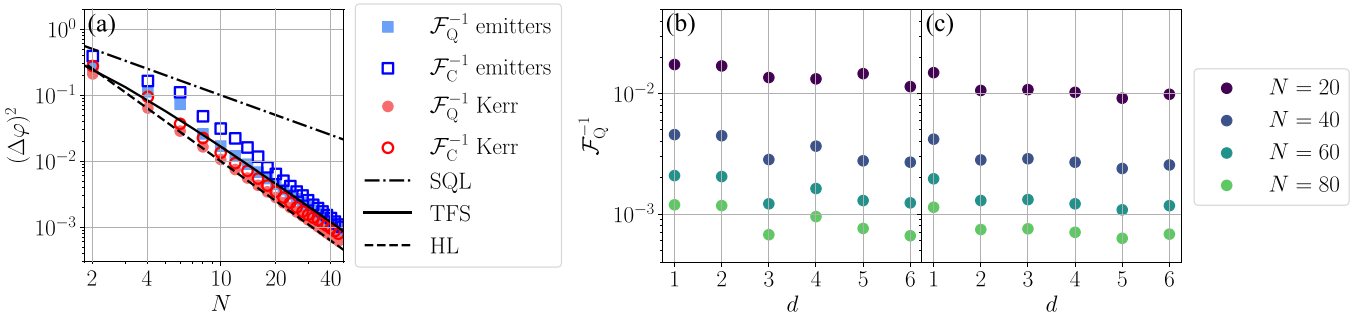

FIG. 7. Results obtained by employing preparation and measurement PQCs with depth $d = 2$. (a) Estimation error $(\Delta\varphi)^2$ in the noiseless scenario as a function of the mean number of photons N. Blue squares (red circles) correspond to the results of the emitters (Kerr) *Ansatz*: filled (void) markers are the inverse of the QFI (CFI) $\mathcal{F}_{\mathrm{Q(C)}}^{-1}$ in the two cases. Dashed-dotted/solid/dashed lines signal the SQL/TFS/HL scaling. (b), (c) Scaling of the inverse of the QFI $\mathcal{F}_{\mathrm{Q}}^{-1}$ as a function of the number of layers d of the PQC, for different values of N. Contrary to Fig. 2 of the main text, these results are calculated by fixing d and employing the optimal parameters for $N-1$ as the initial parameters for N. (b) Emitters *Ansatz*. (c) Kerr *Ansatz*.

system size N, but better than with full tomography. Randomized measurements were also employed in [74] to construct a series of polynomial lower bounds that converge to the QFI.

(3) An additional application of randomized measurements that further simplifies the measurement of several properties of the quantum system is classical shadows [77]. In this approach, the number of measurements to be performed is independent of the system size. In particular, it has been applied to measure the fidelity of a state preparation process [78] leading to higher fidelities with a number of operations orders of magnitude smaller than with maximum-likelihood estimation (which is an incomplete tomography method).

(4) One can also capitalize on the relation that exists between the quantum Fisher information and the variance of the operator generating the parameter encoding [79–81] to estimate the QFI thorough a tight lower bound [82]. This can be applied in large systems while requiring few operator expectation values.

(5) Further approaches to measure the fidelity include the SWAP test [83] and generalizing the quantum switch employed in [84] to measure entanglement entropy.

To sum up, the two-mode nature of our system, whose Hilbert space dimension grows quadratically with the mean photon number, combined with the growing number of techniques to experimentally estimate the fidelity (and thus the QFI) makes us confident about the possibility of implementing our scheme in experimental platforms.

APPENDIX D: PHYSICAL IMPLEMENTATION OF TUNABLE OPTICAL NONLINEARITIES

In this Appendix we discuss in more detail the physical implementation of the tunable optical nonlinearities required by our protocol. The operations in which the two *Ansätze* are based are given by the Trotterization of the natural evolution of quantum states under their respective system's Hamiltonian. This is an example of analog quantum computing [85,86], which is a particularly feasible way to exploit state-of-the-art quantum hardware. Nevertheless, a critical aspect of our work is the access to tunable optical nonlinearities. In the case of the emitters *Ansatz*, tunable emitter-photon interactions can be implemented by addressing an atom featuring a so-called lambda transition with Raman lasers [87,88]. For the Kerr *Ansatz*, tunable Kerr nonlinearities have been implemented in superconducting circuits working in the microwave regime [89,90]. However, it is not so obvious how to achieve a tunable Kerr nonlinearity at optical frequencies, although there is a recent proposal in the few-photon regime based on the coupling of an infrared resonator to intersubband quantum well transition dipoles [91].

However, even in the worst-case scenario in which such tunability cannot be realized, one can simulate the algorithm in a classical computer and then fabricate the desired setup in which fixed nonlinearities accounting for the corresponding optimal values are applied to each mode. This is an example of the *in silicon* approach that we mentioned in the main text. Thus, overall, we do not expect the requirement of tunable interactions to be a bottleneck for the implementation of our proposal.

APPENDIX E: RESULTS FOR $d = 2$

In this Appendix we provide more information on the results for a circuit depth $d = 2$, the convergence of the QFI as a function of the number of layers d of the preparation PQC, and the reason behind choosing $d = 5$ in Figs. 3 and 4 of the main text.

We start by providing the analog of Fig. 3 of the main text but employing a circuit depth $d = 2$ for both the preparation and the measurement PQCs. The results, shown in panel (a) of Fig. 7, are quite similar to those obtained with $d = 5$. Even though the Kerr *Ansatz* is able to produce states reaching the HL for $N \lesssim 20$, above this value they start deviating upwards, giving slightly larger values of $\mathcal{F}_{\mathrm{Q}}^{-1}$, but still very close to the HL. As for the emitters *Ansatz*, for $N \gtrsim 10$ they saturate the TFS scaling. A linear fit reveals that the two *Ansätze* follow $\mathcal{F}_{\mathrm{Q}}^{-1} \sim 1/N^{\beta}$ with $\beta = 1.90$ for the Kerr *Ansatz* and $\beta = 1.93$ for the emitters one. Regarding the CFI, it closely follows the results for the QFI. For the emitters *Ansatz*, this behavior is very similar to what we found for $d = 5$. However, for the Kerr *Ansatz*, the agreement was even better for $d = 5$. In spite of this, with $d = 2$ our VQA is still able to generate states featuring a large metrological advantage, reaching the value of QFI of TFS employing the emitters *Ansatz*, and even beating

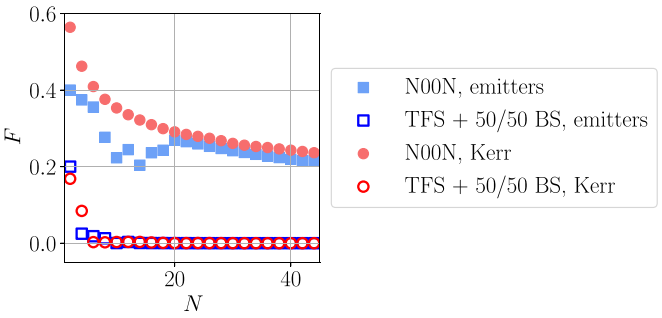

FIG. 8. Fidelity F of the optimal states generated by the preparation PQC after going through a 50/50 beam splitter with respect to NOON states and TFS after passing through a 50/50 beam splitter (TFS + 50/50 BS), for both the emitters and the Kerr *Ansätze*, as a function of the mean number of photons N. All calculations were made employing PQCs with depth $d = 5$.

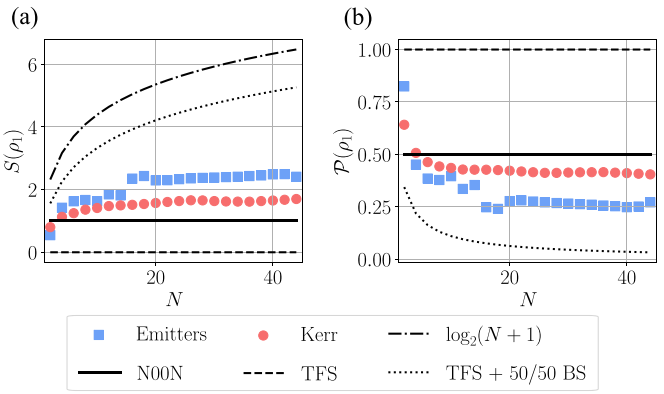

FIG. 9. (a) Von Neumann entropy of entanglement of the reduced density matrix of the first photonic mode $S(\rho_1)$ as a function of the mean number of photons N. The dashed-dotted line shows the maximum entropy $\log_2(N+1)$ for a mode with $N+1$ possible states. (b) Purity of the reduced density matrix of the first photonic mode $\mathcal{P}(\rho_1)$ as a function of the mean number of photons N. In both panels, blue squares (red circles) are the results of the emitters (Kerr) *Ansatz* after passing through the first symmetric (50/50) beam splitter of the MZI. The solid (dashed) lines represent the results for NOON states (TFS), while the dotted lines are obtained with TFS sent through a symmetric beam splitter. All calculations were made employing PQCs with depth $d = 5$.

it and approaching the HL in the case of the Kerr *Ansatz*. This supports our claim of a highly efficient method for the generation of metrologically relevant quantum states.

Now we further clarify why we picked $d = 5$ for Figs. 3 and 4 in the main text. Actually, such figures are calculated differently from Fig. 2. In the latter figure, the total mean-photon number N was fixed and then the data for d was computed using the optimal parameters for $d - 1$ as the new initial parameters. In Figs. 3 and 4, d was fixed and the data for N was computed using the optimal parameters for $N - 1$ as initial parameters. This implies that, for the same value of d, using the latter method more optimizations have been carried for values of $N > d$, which leads to better results than in the former case.

This is visible in panels (b) and (c) of Fig. 7, where we show the analog of Fig. 2 of the main text but carrying the optimization using the latter method (i.e., fixing d and increasing N). The inverse of the QFI $\mathcal{F}_Q^{-1}$ is plotted as a function of the circuit depth d for several values of the mean-photon number N, for the emitters [panel (b)] and the Kerr [panel (c)] *Ansätze*. In the two cases, even with $d = 1$ the VQA gives results which are close to the converged ones presented in Fig. 2 of the main text. As mentioned before, this is a consequence of the larger number of optimizations carried with this method before reaching the value of N considered. For $d > 1$, $\mathcal{F}_Q^{-1}$ oscillates, with some values of d performing better than others. After an exploration of the results obtained with different values of the circuit depth in the range $d = 1$–6, we concluded that PQCs with $d = 5$ attained slightly better results for both *Ansätze*. This is why we employed this value in Figs. 3 and 4 of the main text.

APPENDIX F: PROPERTIES OF THE OUTPUT STATES OF THE VQA

In this Appendix we explore the nature of the optimal states prepared by the VQA and how close they are to NOON states and TFS. In Fig. 8(a) we calculated the fidelity (i.e., the complex modulus of the scalar product between two quantum states) of the states generated by the emitters and Kerr *Ansätze* in the preparation stage of the VQA (with depth $d = 5$) after going through the first symmetric (50/50) beam splitter of the MZI with respect to TFS after passing through the same symmetric beam splitter (TFS + 50/50 BS) as well as with respect to NOON states. This is the correct comparison as TFS are defined prior to entering the first beam splitter of the MZI interferometer, while NOON states are directly sent through the phase encoding. As one can see, as N grows, the fidelities with respect to TFS + 50/50 BS rapidly decay to zero. On the other hand, the fidelities with respect to NOON states are finite even for large values of N. This is true for both *Ansätze*. In other words, the states generated by our VQA hold some similarity with NOON states even for mean-photon numbers $N \gtrsim 40$. The fact that they share a relatively low fidelity ($F \simeq 0.2$–0.25 for $N \simeq 40$) should not be disturbing, as metrological advantage can be obtained with a variety of different states. Besides, our VQA does not employ the fidelity with respect to a target state as cost function, but rather aims to maximize the QFI without caring about the particular state obtained.

In order to further dive into the nature of the optimal states produced by our VQA, an interesting benchmark is to address whether there is entanglement between the two photonic modes (similar to what happens in a NOON state) or if both of them are uncorrelated (like in TFS). To explore this, we calculated the Von Neumann entropy of entanglement [shown in Fig. 9(a)] as well as the purity of the reduced density matrix [see Fig. 9(b)] of the first photonic mode.

We start from the density matrix describing the two photonic modes of our system ρ_{phot}. In the case of the emitters *Ansatz*, such density matrix can be obtained by tracing out the emitters degrees of freedom, i.e., $\rho_{\text{phot}} = \text{Tr}_{\text{emit}}\{\rho\}$, where ρ is the density matrix describing the total system of photons and emitters. At this point, and without loss of generality, we can trace out the second photonic mode, obtaining $\rho_1 =$

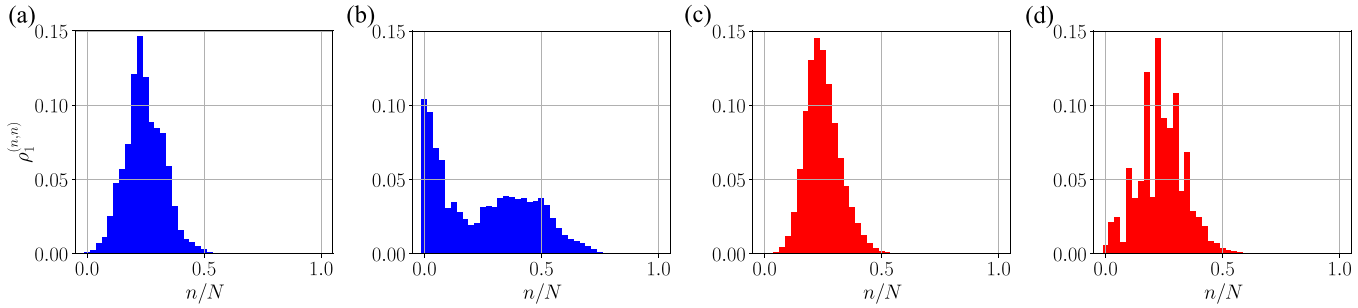

FIG. 10. Diagonal elements of the reduced density matrix of the first photonic mode $\rho_1^{(n,n)}$ as a function of the number of photons in that mode n. The total number of photons is fixed at $N = 20$. (a) Optimal state maximizing the QFI prepared using the emitters *Ansatz*. (b) Optimal state maximizing the CFI prepared using the emitters *Ansatz*. (c) Optimal state maximizing the QFI prepared using the Kerr *Ansatz*. (d) Optimal state maximizing the CFI prepared using the Kerr *Ansatz*. All calculations were made employing PQCs with depth $d = 5$.

$\mathrm{Tr}_2\{\rho_{\mathrm{phot}}\}$. The entropy of entanglement is given by [92]

$$S(\rho_1) = -\mathrm{Tr}(\rho_1 \log_2 \rho_1), \tag{F1}$$

or equivalently by

$$S(\rho_1) = -\sum_i \lambda_i \log_2(\lambda_i), \tag{F2}$$

where $\{\lambda_i\}$ is the set of M eigenvalues of ρ_1 and the sum above runs from $i = 1$ to $i = M$.

The results obtained with the states generated by the emitters and the Kerr *Ansätze* are shown in Fig. 9(a) (again, taking such states after they have gone through the first 50/50 beam splitter of the MZI). These are benchmarked against the values of the entropy of entanglement for TFS [which are separable and thus give $S(\rho_1) = 0$], NOON states [in which only two states are entangled, and thus $S(\rho_1) = \log_2(2) = 1$], TFS going through a symmetric (50/50) beam splitter (for which all possible combinations featuring an even number of photons are entangled), and the maximum possible value $S(\rho_1) = \log_2(N + 1)$ for $N + 1$ available quantum states. As the mean number of photons N increases, the values of $S(\rho_1)$ obtained with the two *Ansätze* increase following a logarithmic law, surpassing the entropy of entanglement of NOON states as soon as for $N = 4$, although their values lie below those obtained by TFS passing through a symmetric beam splitter. This is telling us that both *Ansätze* are generating entanglement between the two photonic modes. Therefore, tunneling between the two modes is a crucial resource for the *Ansätze*. This also confirms that the optimal states of our formalism do not resemble TFS.

A similar metric addressing the entanglement between the two photonic modes is the purity of the first photonic mode, i.e.,

$$\mathcal{P}(\rho_1) = \mathrm{Tr}\{\rho_1^2\}. \tag{F3}$$

Since a pure state always satisfies $\mathcal{P} = 1$, if there is no entanglement between the two photonic modes we should obtain $\mathcal{P}(\rho_1) = 1$. On the contrary, this value will be lower than 1 if entanglement is present.

The results are shown in Fig. 9(b), and they go along the lines of Fig. 9(a): the purity of states generated by the two *Ansätze* (as before, taking such states after they have gone through the first 50/50 beam splitter of the MZI) rapidly diminishes as N increases. The obtained values of $\mathcal{P}(\rho_1)$ are below 1, signaling that the resulting ρ_1 is a mixed state for both *Ansätze* and that the two photonic modes are entangled. These results are benchmarked with the values of $\mathcal{P}(\rho_1)$ resulting from NOON states, TFS, and TFS going through a symmetric beam splitter. As one can expect from Fig. 9(a), the optimal states found with our VQA provide values of the purity between those of NOON states and TFS passing through the beam splitter.

Overall, the results presented in this Appendix confirm that the two *Ansätze* are generating states that are different from the NOON and TFS, and also different between them.

Finally, in Fig. 10 we plotted the diagonal terms of the reduced density matrix of the first photonic mode $\rho_1^{(n,n)}$ in the Fock states basis $|n\rangle$, where n is the number of photons in that mode, after going through the preparation (a), (c) and measurement (b), (d) PQCs. We fixed the mean number of photons at $N = 20$. Panels (a), (b) show the results for the emitters *Ansatz*, while panels (c), (d) display those obtained with the Kerr one. As one can see, the optimal probe states given by the preparation stage are already different from coherent states, which would feature a Poisson distribution. Moreover, the measurement PQC further modifies the shape of the states.

Regarding the effect of noise, we have checked that the states prepared by our VQA still feature similar properties for finite values of κ.

APPENDIX G: OPTIMAL PARAMETERS

In this Appendix we examine the optimal parameters $\boldsymbol{\theta}_{\mathrm{opt}}$ and $\boldsymbol{\mu}_{\mathrm{opt}}$ obtained by the classical optimizer in the noiseless case ($\kappa = 0$), for preparation and measurement PQCs with depth $d = 5$, and for $N = 20$ photons. The aim is to make sure that the parameters maximizing the QFI and the CFI can be attained in real experimental platforms. This is especially concerning for the variational parameters $\tilde{g}$ and $\tilde{U}$, which encode correspondingly the interaction strength in the emitters and Kerr *Ansatz* and are of the order of g/κ and U/κ, respectively. Figures 11(a)–11(c) show the values of $\tilde{J}$, $\tilde{\Delta}$, and $\tilde{g}$ obtained with the emitters *Ansatz*. As one can see, the maximum value of the emitter-photon coupling required is $|g|/\kappa \simeq 5$. This can be realized in state-of-the-art cavity-QED experiments [56–60].

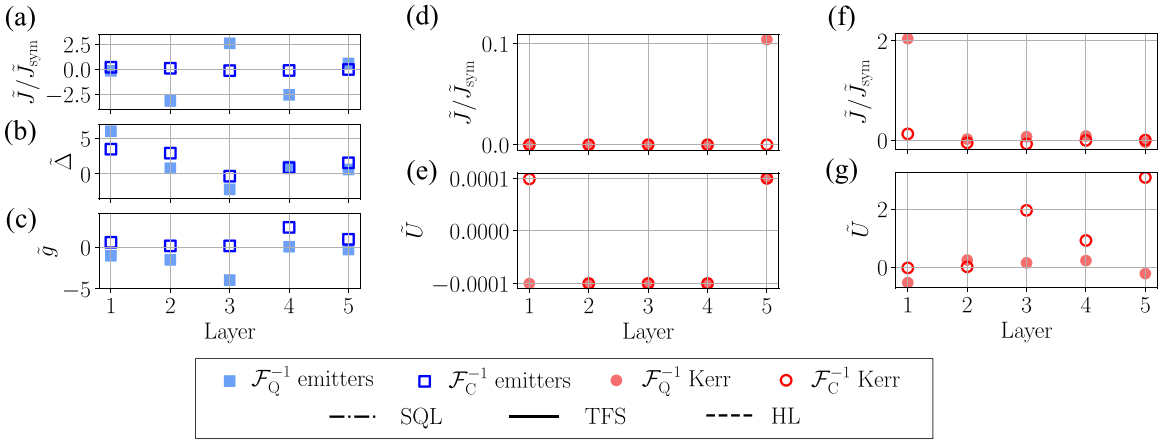

FIG. 11. Optimal parameters $\boldsymbol{\theta}_{\text{opt}}$ and $\boldsymbol{\mu}_{\text{opt}}$ for the noiseless ($\kappa = 0$) case with $N = 20$ and a circuit depth $d = 5$. (a) Emitters *Ansatz*. (b) Kerr *Ansatz* with $\tilde{U}_{\text{bound}} = 10^{-4}$. (c) Unbound Kerr *Ansatz*. The tunneling parameter $\tilde{J}$ is plotted in units of that of a symmetric beam splitter $\tilde{J}_{\text{sym}} = \pi/4$.

Regarding the Kerr *Ansatz*, we have to distinguish between the behavior below and above the expressibility threshold shown in Fig. 3(b) of the main text. Therefore, we compare the results for a Kerr nonlinearity bound $\tilde{U}_{\text{bound}} = 10^{-4}$ [shown in Figs. 11(d) and 11(e)] with those for a boundless nonlinearity [shown in Figs. 11(f) and 11(g)]. As we can see, in the first case the optimal values of $|\tilde{U}|$ given by the optimizer saturate $|\tilde{U}_{\text{bound}}|$ for all layers, thus signaling that the Kerr nonlinearity bound is forcing the optimizer to stay in a restricted region of the Hilbert space where it cannot find the global minimum of the cost function, and therefore limiting its expressibility.

However, once we eliminate the Kerr nonlinearity bound, we see in Fig. 11(g) that the optimal parameters contain values of $U/\kappa \sim 1$. In a real experiment, this would require microwave platforms, which are capable of reaching $U/\kappa \sim 10^2$ [63–65]. However, going above the expressibility threshold may be also within the reach of systems working in the optical regime, as the current limit in $U/\kappa \sim 10^{-2}$ [61] lies just in the middle of the $\tilde{U}_{\text{bound}}$ threshold.

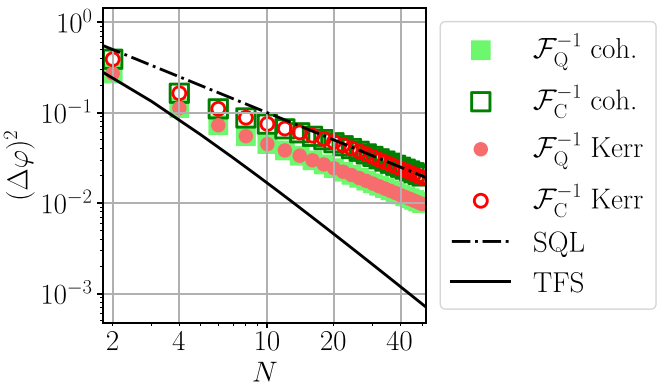

FIG. 12. Estimation error $(\Delta\varphi)^2$ as a function of the mean number of photons N for the Kerr *Ansatz* with $\tilde{U}_{\text{bound}} = 10^{-4}$ and a circuit depth $d = 5$, as well as for two input coherent states with mean photon number $|\alpha|^2 = N/2$ without the preparation and measurement PQCs.

APPENDIX H: KERR *ANSATZ* BELOW THE NONLINEARITY THRESHOLD

In this Appendix we apply our VQA to a Kerr *Ansatz* featuring a nonlinearity bound $\tilde{U}_{\text{bound}} = 10^{-4}$, i.e., below the expressibility threshold, and in the noiseless case ($\kappa = 0$). We will show that such bound *Ansatz* is unable to provide a quantum advantage. Figure 12 shows the results of our VQA for the inverse of the QFI ($\mathcal{F}_Q^{-1}$) and the CFI ($\mathcal{F}_C^{-1}$) as a function of N. As one can see, although the inverse of the QFI lies slightly below the SQL, it follows the same $1/N$ scaling, while the CFI does not reach the corresponding values of QFI and follows the SQL. A circuit depth $d = 5$ was employed. These are the same results that are obtained employing coherent states with $\alpha = N/2$ at the input of the MZI and removing the preparation and measurement PQCs (i.e., taking $\boldsymbol{\theta} = \boldsymbol{\mu} = 0$). This supports the results shown in Fig. 11(e) of Appendix G, signaling that having a $\tilde{U}$ above the threshold in $\tilde{U}_{\text{bound}}$ is indispensable to allow the classical optimizer to explore the region of the Hilbert space where solutions that feature a quantum advantage can be found.

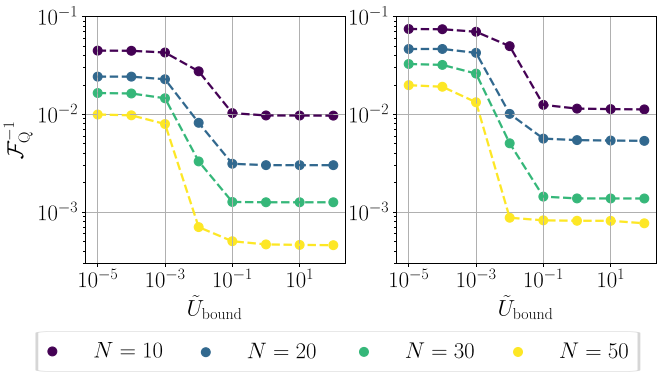

FIG. 13. Inverse of the QFI $\mathcal{F}_Q^{-1}$ (a) and CFI $\mathcal{F}_C^{-1}$ (b) for the Kerr *Ansatz* as a function of the bound in the Kerr nonlinearity strength $\tilde{U}_{\text{bound}}$ for several values of the mean number of photons N. All calculations were made employing PQCs with depth $d = 5$.

APPENDIX I: CRITICAL BOUND FOR DIFFERENT PHOTON NUMBERS

In this Appendix we study the dependence of the critical value of $\tilde{U}_{\text{bound}}$ above which the Kerr nonlinearity *Ansatz* is able to provide optimal solutions with respect to the mean number of photons N. To do it, in Fig. 13 we plot the equivalent of Fig. 3(b) of the main text for several values of N. As one can see, the crossover between the two regimes takes place around $\tilde{U}_{\text{bound}} = 10^{-2}$ independent of N for both the QFI [panel (a)] and the CFI [panel (b)]. A circuit depth $d = 5$ was employed throughout all these calculations.

[1] J. J. Bollinger, W. M. Itano, D. J. Wineland, and D. J. Heinzen, Optimal frequency measurements with maximally correlated states, Phys. Rev. A **54**, R4649 (1996).

[2] D. Leibfried, M. D. Barrett, T. Schaetz, J. Britton, J. Chiaverini, W. M. Itano, J. D. Jost, C. Langer, and D. J. Wineland, Toward Heisenberg-limited spectroscopy with multiparticle entangled states, Science **304**, 1476 (2004).

[3] V. Giovannetti, S. Lloyd, and L. Maccone, Quantum-enhanced measurements: Beating the standard quantum limit, Science **306**, 1330 (2004).

[4] V. Giovannetti, S. Lloyd, and L. Maccone, Quantum metrology, Phys. Rev. Lett. **96**, 010401 (2006).

[5] V. Giovannetti, S. Lloyd, and L. Maccone, Advances in quantum metrology, Nat. Photon. **5**, 222 (2011).

[6] G. Tóth and I. Apellaniz, Quantum metrology from a quantum information science perspective, J. Phys. A: Math. Theor. **47**, 424006 (2014).

[7] C. L. Degen, F. Reinhard, and P. Cappellaro, Quantum sensing, Rev. Mod. Phys. **89**, 035002 (2017).

[8] J. P. Dowling and K. P. Seshadreesan, Quantum optical technologies for metrology, sensing, and imaging, J. Lightwave Technol. **33**, 2359 (2015).

[9] R. Demkowicz-Dobrzański, M. Jarzyna, and J. Kołodyński, *Quantum Limits in Optical Interferometry* (Elsevier, Amsterdam, 2015), Chap. 4, pp. 345–435.

[10] S. Pirandola, B. R. Bardhan, T. Gehring, C. Weedbrook, and S. Lloyd, Advances in photonic quantum sensing, Nat. Photon. **12**, 724 (2018).

[11] E. Polino, M. Valeri, N. Spagnolo, and F. Sciarrino, Photonic quantum metrology, AVS Quantum Sci. **2**, 024703 (2020).

[12] M. J. Holland and K. Burnett, Interferometric detection of optical phase shifts at the Heisenberg limit, Phys. Rev. Lett. **71**, 1355 (1993).

[13] R. A. Campos, C. C. Gerry, and A. Benmoussa, Optical interferometry at the Heisenberg limit with twin Fock states and parity measurements, Phys. Rev. A **68**, 023810 (2003).

[14] I. Afek, O. Ambar, and Y. Silberberg, High-noon states by mixing quantum and classical light, Science **328**, 879 (2010).

[15] Y. Israel, I. Afek, S. Rosen, O. Ambar, and Y. Silberberg, Experimental tomography of noon states with large photon numbers, Phys. Rev. A **85**, 022115 (2012).

[16] L. A. Rozema, J. D. Bateman, D. H. Mahler, R. Okamoto, A. Feizpour, A. Hayat, and A. M. Steinberg, Scalable spatial superresolution using entangled photons, Phys. Rev. Lett. **112**, 223602 (2014).

[17] K. Vogel, V. M. Akulin, and W. P. Schleich, Quantum state engineering of the radiation field, Phys. Rev. Lett. **71**, 1816 (1993).

[18] C. K. Law and J. H. Eberly, Arbitrary control of a quantum electromagnetic field, Phys. Rev. Lett. **76**, 1055 (1996).

[19] A. González-Tudela, V. Paulisch, D. E. Chang, H. J. Kimble, and J. I. Cirac, Deterministic generation of arbitrary photonic states assisted by dissipation, Phys. Rev. Lett. **115**, 163603 (2015).

[20] M. Uria, P. Solano, and C. Hermann-Avigliano, Deterministic generation of large fock states, Phys. Rev. Lett. **125**, 093603 (2020).

[21] M. Uria, A. Maldonado-Trapp, C. Hermann-Avigliano, and P. Solano, Emergence of non-Gaussian coherent states through nonlinear interactions, Phys. Rev. Res. **5**, 013165 (2023).

[22] C. Guerlin, J. Bernu, S. Deléglise, C. Sayrin, S. Gleyzes, S. Kuhr, M. Brune, J.-M. Raimond, and S. Haroche, Progressive field-state collapse and quantum non-demolition photon counting, Nature (London) **448**, 889 (2007).

[23] S. Deléglise, I. Dotsenko, C. Sayrin, J. Bernu, M. Brune, J.-M. Raimond, and S. Haroche, Reconstruction of non-classical cavity field states with snapshots of their decoherence, Nature (London) **455**, 510 (2008).

[24] C. Sayrin, I. Dotsenko, X. Zhou, B. Peaudecerf, T. Rybarczyk, S. Gleyzes, P. Rouchon, M. Mirrahimi, H. Amini, M. Brune, J.-M. Raimond, and S. Haroche, Real-time quantum feedback prepares and stabilizes photon number states, Nature (London) **477**, 73 (2011).

[25] X. Deng, S. Li, Z.-J. Chen, Z. Ni, Y. Cai, J. Mai, L. Zhang, P. Zheng, H. Yu, C.-L. Zou, S. Liu, F. Yan, Y. Xu, and D. Yu, Heisenberg-limited quantum metrology using 100-photon Fock states, arXiv:2306.16919 [quant-ph].

[26] P. Kok, H. Lee, and J. P. Dowling, Creation of large-photon-number path entanglement conditioned on photodetection, Phys. Rev. A **65**, 052104 (2002).

[27] P. Walther, J.-W. Pan, M. Aspelmeyer, R. Ursin, S. Gasparoni, and A. Zeilinger, De Broglie wavelength of a non-local four-photon state, Nature (London) **429**, 158 (2004).

[28] X. L. Wang, L. K. Chen, W. Li, H. L. Huang, C. Liu, C. Chen, Y. H. Luo, Z. E. Su, D. Wu, Z. D. Li, H. Lu, Y. Hu, X. Jiang, C. Z. Peng, L. Li, N. L. Liu, Y. A. Chen, C. Y. Lu, and J. W. Pan, Experimental ten-photon entanglement, Phys. Rev. Lett. **117**, 210502 (2016).

[29] H. Wang, J. Qin, X. Ding, M. C. Chen, S. Chen, X. You, Y. M. He, X. Jiang, L. You, Z. Wang, C. Schneider, J. J. Renema, S. Höfling, C. Y. Lu, and J. W. Pan, Boson sampling with 20 input photons and a 60-mode interferometer in a 1014-dimensional Hilbert space, Phys. Rev. Lett. **123**, 250503 (2019).

[30] M. Cerezo, A. Arrasmith, R. Babbush, S. C. Benjamin, S. Endo, K. Fujii, J. R. McClean, K. Mitarai, X. Yuan, L. Cincio, and P. J. Coles, Variational quantum algorithms, Nat. Rev. Phys. **3**, 625 (2021).

[31] K. Bharti, A. Cervera-Lierta, T. H. Kyaw, T. Haug, S. Alperin-Lea, A. Anand, M. Degroote, H. Heimonen, J. S. Kottmann, T. Menke, W. K. Mok, S. Sim, L. C. Kwek, and A. Aspuru-Guzik,

Noisy intermediate-scale quantum algorithms, Rev. Mod. Phys. **94**, 015004 (2022).

[32] R. Kaubruegger, P. Silvi, C. Kokail, R. van Bijnen, A. M. Rey, J. Ye, A. M. Kaufman, and P. Zoller, Variational spin-squeezing algorithms on programmable quantum sensors, Phys. Rev. Lett. **123**, 260505 (2019).

[33] Z.-H. Sun, Y.-Y. Wang, Y.-R. Zhang, F. Nori, and H. Fan, Variational generation of spin squeezing on one-dimensional quantum devices with nearest-neighbor interactions, Phys. Rev. Res. **5**, 043285 (2023).

[34] J. J. Meyer, J. Borregaard, and J. Eisert, A variational toolbox for quantum multi-parameter estimation, npj Quantum Inf. **7**, 89 (2021).

[35] Z. Ma, P. Gokhale, T.-X. Zheng, S. Zhou, X. Yu, L. Jiang, P. Maurer, and F. T. Chong, Adaptive circuit learning for quantum metrology, in *Proceedings of the 2021 IEEE International Conference on Quantum Computing and Engineering* (IEEE, New York, 2021), p. 419.

[36] T. K. Le, H. Q. Nguyen, and L. B. Ho, Variational quantum metrology for multiparameter estimation under dephasing noise, arXiv:2305.08289 [quant-ph].

[37] B. Koczor, S. Endo, T. Jones, Y. Matsuzaki, and S. C. Benjamin, Variational-state quantum metrology, New J. Phys. **22**, 083038 (2020).

[38] J. L. Beckey, M. Cerezo, A. Sone, and P. J. Coles, Variational quantum algorithm for estimating the quantum fisher information, Phys. Rev. Res. **4**, 013083 (2022).

[39] J. Yang, S. Pang, Z. Chen, A. N. Jordan, and A. del Campo, Variational principle for optimal quantum controls in quantum metrology, Phys. Rev. Lett. **128**, 160505 (2022).

[40] R. Kaubruegger, A. Shankar, D. V. Vasilyev, and P. Zoller, Optimal and variational multiparameter quantum metrology and vector-field sensing, PRX Quantum **4**, 020333 (2023).

[41] T. Krisnanda, S. Ghosh, T. Paterek, and T. C. Liew, Creating and concentrating quantum resource states in noisy environments using a quantum neural network, Neural Netw. **136**, 141 (2021).

[42] V. Cimini, M. Valeri, S. Piacentini, F. Ceccarelli, G. Corrielli, R. Osellame, N. Spagnolo, and F. Sciarrino, Variational quantum algorithm for experimental photonic multiparameter estimation, arXiv:2308.02643 [quant-ph].

[43] G. R. Steinbrecher, J. P. Olson, D. Englund, and J. Carolan, Quantum optical neural networks, npj Quantum Inf. **5**, 60 (2019).

[44] H. J. Kimble, Strong interactions of single atoms and photons in cavity QED, Phys. Scr. **T76**, 127 (1998).

[45] M. B. On, F. Ashtiani, D. Sanchez-Jacome, D. Perez-Lopez, S. J. B. Yoo, and A. Blanco-Redondo, Programmable integrated photonics for topological hamiltonians, Nat. Commun. **15**, 629 (2024).

[46] S.-N. Sun, M. Motta, R. N. Tazhigulov, A. T. K. Tan, G. K.-L. Chan, and A. J. Minnich, Quantum computation of finite-temperature static and dynamical properties of spin systems using quantum imaginary time evolution, PRX Quantum **2**, 010317 (2021).

[47] Codes to reproduce the results of this manuscript are available at https://github.com/albertomdlh/quantum-metrology-variational.

[48] C. Gerry and P. Knight, *Introductory Quantum Optics* (Cambridge University Press, Cambridge, UK, 2005).

[49] This choice of initial states is motivated by the ease with which coherent states can be experimentally prepared. In Appendix B we also consider squeezed coherent states as inputs, but there was no significant improvement over the results.

[50] M. Cramer, M. B. Plenio, S. T. Flammia, R. Somma, D. Gross, S. D. Bartlett, O. Landon-Cardinal, D. Poulin, and Y.-K. Liu, Efficient quantum state tomography, Nat. Commun. **1**, 149 (2010).

[51] H. Walther, B. T. H. Varcoe, B.-G. Englert, and T. Becker, Cavity quantum electrodynamics, Rep. Prog. Phys. **69**, 1325 (2006).

[52] A. Reiserer and G. Rempe, Cavity-based quantum networks with single atoms and optical photons, Rev. Mod. Phys. **87**, 1379 (2015).

[53] A. Blais, A. L. Grimsmo, S. M. Girvin, and A. Wallraff, Circuit quantum electrodynamics, Rev. Mod. Phys. **93**, 025005 (2021).

[54] P. N. Butcher and D. Cotter, *The Elements of Nonlinear Optics*, Cambridge Studies in Modern Optics (Cambridge University Press, Cambridge, UK, 1990).

[55] In Figs. 3 and 4 we employ a circuit depth $d = 5$ larger than the number of layers $d = 2$ necessary to attain convergence because we found a slight improvement with respect to the latter case. Results for $d = 2$ can be found in Appendix E.

[56] X. Gu, A. F. Kockum, A. Miranowicz, Y. xi Liu, and F. Nori, Microwave photonics with superconducting quantum circuits, Phys. Rep. **718-719**, 1 (2017).

[57] D. Meschede, H. Walther, and G. Müller, One-atom maser, Phys. Rev. Lett. **54**, 551 (1985).

[58] R. J. Thompson, G. Rempe, and H. J. Kimble, Observation of normal-mode splitting for an atom in an optical cavity, Phys. Rev. Lett. **68**, 1132 (1992).

[59] P. Lodahl, S. Mahmoodian, and S. Stobbe, Interfacing single photons and single quantum dots with photonic nanostructures, Rev. Mod. Phys. **87**, 347 (2015).

[60] C. S. M. noz, F. P. Laussy, E. del Valle, C. Tejedor, and A. González-Tudela, Filtering multiphoton emission from state-of-the-art cavity quantum electrodynamics, Optica **5**, 14 (2018).

[61] A. Delteil, T. Fink, A. Schade, S. Höfling, C. Schneider, and A. İmamoglu, Towards polariton blockade of confined exciton–polaritons, Nat. Mater. **18**, 219 (2019).

[62] G. Muñoz-Matutano, A. Wood, M. Johnsson, X. Vidal, B. Q. Baragiola, A. Reinhard, A. Lemaître, J. Bloch, A. Amo, G. Nogues, B. Besga, M. Richard, and T. Volz, Emergence of quantum correlations from interacting fibre-cavity polaritons, Nat. Mater. **18**, 213 (2019).

[63] J. Koch, T. M. Yu, J. Gambetta, A. A. Houck, D. I. Schuster, J. Majer, A. Blais, M. H. Devoret, S. M. Girvin, and R. J. Schoelkopf, Charge-insensitive qubit design derived from the cooper pair box, Phys. Rev. A **76**, 042319 (2007).

[64] G. Kirchmair, B. Vlastakis, Z. Leghtas, S. E. Nigg, H. Paik, E. Ginossar, M. Mirrahimi, L. Frunzio, S. M. Girvin, and R. J. Schoelkopf, Observation of quantum state collapse and revival due to the single-photon Kerr effect, Nature (London) **495**, 205 (2013).

[65] S. Puri, C. K. Andersen, A. L. Grimsmo, and A. Blais, Quantum annealing with all-to-all connected nonlinear oscillators, Nat. Commun. **8**, 15785 (2017).

[66] C. Gardiner and P. Zoller, *Quantum Noise: A Handbook of Markovian and Non-Markovian Quantum Stochastic Methods*

with Applications to Quantum Optics, Springer Series in Synergetics (Springer, Berlin, 2004).

[67] R. Demkowicz-Dobrzański, J. Kołodyński, and M. GuŢă, The elusive Heisenberg limit in quantum-enhanced metrology, Nat. Commun. **3**, 1063 (2012).

[68] U. Dorner, R. Demkowicz-Dobrzanski, B. J. Smith, J. S. Lundeen, W. Wasilewski, K. Banaszek, and I. A. Walmsley, Optimal quantum phase estimation, Phys. Rev. Lett. **102**, 040403 (2009).

[69] M. Brownnutt, M. Kumph, P. Rabl, and R. Blatt, Ion-trap measurements of electric-field noise near surfaces, Rev. Mod. Phys. **87**, 1419 (2015).

[70] M.-D. Choi, Completely positive linear maps on complex matrices, Linear Alg. Appl. **10**, 285 (1975).

[71] R. Jozsa, Fidelity for mixed quantum states, J. Mod. Opt. **41**, 2315 (1994).

[72] M. J. D. Powell, A direct search optimization method that models the objective and constraint functions by linear interpolation, in *Advances in Optimization and Numerical Analysis* (Springer Netherlands, Dordrecht, 1994), pp. 51–67.

[73] R. Schnabel, Squeezed states of light and their applications in laser interferometers, Phys. Rep. **684**, 1 (2017).

[74] V. Vitale, A. Rath, P. Jurcevic, A. Elben, C. Branciard, and B. Vermersch, Estimation of the quantum Fisher information on a quantum processor, arXiv:2307.16882 [quant-ph].

[75] S. Ahmed, C. Sánchez Muñoz, F. Nori, and A. F. Kockum, Quantum state tomography with conditional generative adversarial networks, Phys. Rev. Lett. **127**, 140502 (2021).

[76] A. Elben, S. T. Flammia, H.-Y. Huang, R. Kueng, J. Preskill, B. Vermersch, and P. Zoller, The randomized measurement toolbox, Nat. Rev. Phys. **5**, 9 (2023).

[77] H.-Y. Huang, R. Kueng, and J. Preskill, Predicting many properties of a quantum system from very few measurements, Nat. Phys. **16**, 1050 (2020).

[78] G. I. Struchalin, Y. A. Zagorovskii, E. V. Kovlakov, S. S. Straupe, and S. P. Kulik, Experimental estimation of quantum state properties from classical shadows, PRX Quantum **2**, 010307 (2021).

[79] G. Tóth and D. Petz, Extremal properties of the variance and the quantum Fisher information, Phys. Rev. A **87**, 032324 (2013).

[80] G. Toth, Lower bounds on the quantum Fisher information based on the variance and various types of entropies, arXiv:1701.07461 [quant-ph].

[81] G. Tóth and F. Fröwis, Uncertainty relations with the variance and the quantum Fisher information based on convex decompositions of density matrices, Phys. Rev. Res. **4**, 013075 (2022).

[82] I. Apellaniz, M. Kleinmann, O. Gühne, and G. Tóth, Optimal witnessing of the quantum Fisher information with few measurements, Phys. Rev. A **95**, 032330 (2017).

[83] H. Buhrman, R. Cleve, J. Watrous, and R. de Wolf, Quantum fingerprinting, Phys. Rev. Lett. **87**, 167902 (2001).

[84] D. A. Abanin and E. Demler, Measuring entanglement entropy of a generic many-body system with a quantum switch, Phys. Rev. Lett. **109**, 020504 (2012).

[85] T. H. Johnson, S. R. Clark, and D. Jaksch, What is a quantum simulator? EPJ Quantum Technol. **1**, 10 (2014).

[86] A. J. Daley, I. Bloch, C. Kokail, S. Flannigan, N. Pearson, M. Troyer, and P. Zoller, Practical quantum advantage in quantum simulation, Nature (London) **607**, 667 (2022).

[87] D. J. Wineland, C. Monroe, W. M. Itano, D. Leibfried, B. E. King, and D. M. Meekhof, Experimental issues in coherent quantum-state manipulation of trapped atomic ions, J. Res. Natl. Inst. Stand. Tech. **103**, 259 (1998).

[88] D. J. Alton, N. P. Stern, T. Aoki, H. Lee, E. Ostby, K. J. Vahala, and H. J. Kimble, Strong interactions of single atoms and photons near a dielectric boundary, Nat. Phys. **7**, 159 (2011).

[89] N. E. Frattini, U. Vool, S. Shankar, A. Narla, K. M. Sliwa, and M. H. Devoret, 3-wave mixing Josephson dipole element, Appl. Phys. Lett. **110**, 222603 (2017).

[90] X. L. He, Y. Lu, D. Q. Bao, H. Xue, W. B. Jiang, Z. Wang, A. F. Roudsari, P. Delsing, J. S. Tsai, and Z. R. Lin, Fast generation of Schrödinger cat states using a Kerr-tunable superconducting resonator, Nat. Commun. **14**, 6358 (2023).

[91] M. Arias, J. F. Triana, A. Delgado, and F. Herrera, Coherent anharmonicity transfer from matter to light in the THz regime, New J. Phys. **26**, 013003 (2024).

[92] J. Eisert, M. Cramer, and M. B. Plenio, *Colloquium*: Area laws for the entanglement entropy, Rev. Mod. Phys. **82**, 277 (2010).